

SCIENTIFIC REPORTS



OPEN

Quantum mixed phases of a two-dimensional polarized degenerate Fermi gas in an optical cavity

Yanlin Feng^{1,2}, Kuang Zhang^{1,2}, Jingtao Fan^{1,2}, Feng Mei^{1,2}, Gang Chen^{1,2} & Suotang Jia^{1,2}

The coupling of ultracold fermions to a high-finesse optical cavity can result in novel many-body phenomena, and has attracted significant interests at present. Here we consider a realization of the Fermi-Dicke model with controllable parameters, based on a two-dimensional polarized degenerate Fermi gas coupled to an optical cavity. We analytically investigate the ground-state properties of such system under the mean-field approximation. We find the system can exhibit a rich phase diagram depending on the fermion-photon coupling strength and the atomic resonant frequency. Contrasting to the bosonic counterpart, a first-order quantum phase transition between the superradiant phase and the normal phase featuring two Fermi surfaces can occur for the weak atomic resonant frequency, and there is a unique mixed phase where this normal phase and the superradiant phase coexist. The experimental detection of our results is also discussed.

Cavity quantum electrodynamics (QED) systems, which remarkably illuminate the fundamental interaction between light and matter, have emerged as a novel platform to explore the many-body physics, and promise potential applications in quantum information processing and quantum computing. Recently, the coupling of a Bose-Einstein condensate to a high-finesse optical cavity has been experimentally achieved^{1–8}, thus opens a new avenue that combines cavity QED with ultracold atoms. In particular, the bosonic atoms occupying the same quantum state can interact identically with a single-mode quantized field, which can result in a strong collective matter-field interaction. This has led to the remarkable experimental observation^{3–5} of the celebrated second-order quantum phase transition from the normal phase to the superradiant (SR) phase predicted more than 40 years ago^{9,10}. Cavities moreover allow unconventional dynamical optical potentials which can induce a rich variety of strongly correlated many-body phenomena¹¹.

While current cavity QED experiments have focused on bosons, there are surging interests in exploring the novel physics arising from the coupling of ultracold fermions to the optical cavity^{12–25}. Unlike bosons, fermions obey the Pauli exclusion principle, and two fermions with weak attractive interaction can form Cooper pairs which are responsible for superconductivity²⁶. By coupling ultracold fermions to a high-finesse optical cavity, exotic phenomena have been predicted to arise. For example, recent studies on spinless fermions in the cavity-induced dynamical optical potential have revealed the crucial role of the Fermi statistics on the SR phase transition at moderate and high densities^{17–19}. It has been shown that the cavity-assisted spin-orbit coupling^{27,28} can induce a topological SR phase²⁰. Moreover, the cavity-induced artificial magnetic field²², chiral phases²³, and non-trivial topological states²⁴ have been reported. Interestingly, when fermions in an infinite lattice are gauge coupled to a cavity mode, a SR phase exhibiting a directed particle flow is found to arise above an infinitesimal pumping threshold²⁵.

In this report, we consider a two-dimensional (2D) polarized degenerate Fermi gas coupled to a high-finesse optical cavity and realize a Fermi-Dicke model. Our setup relies on two Raman transitions induced by the quantized cavity field and two transverse pumping lasers, and allows for flexible controllability of the Hamiltonian parameters, including the fermion-photon coupling strength and the effective Zeeman field represented by the atomic resonant frequency. Based on this microscopic model, we study the ground state under the mean-field approximation and find several distinct properties compared to its bosonic counterpart^{9,10}. In particular, we predict a first-order quantum phase transition between the SR phase and the normal phase

¹State Key Laboratory of Quantum Optics and Quantum Optics Devices, Institute of Laser spectroscopy, Shanxi University, Taiyuan, 030006, China. ²Collaborative Innovation Center of Extreme Optics, Shanxi University, Taiyuan, Shanxi, 030006, China. Correspondence and requests for materials should be addressed to F.M. (email: raulmei@163.com) or G.C. (email: chengang971@163.com)

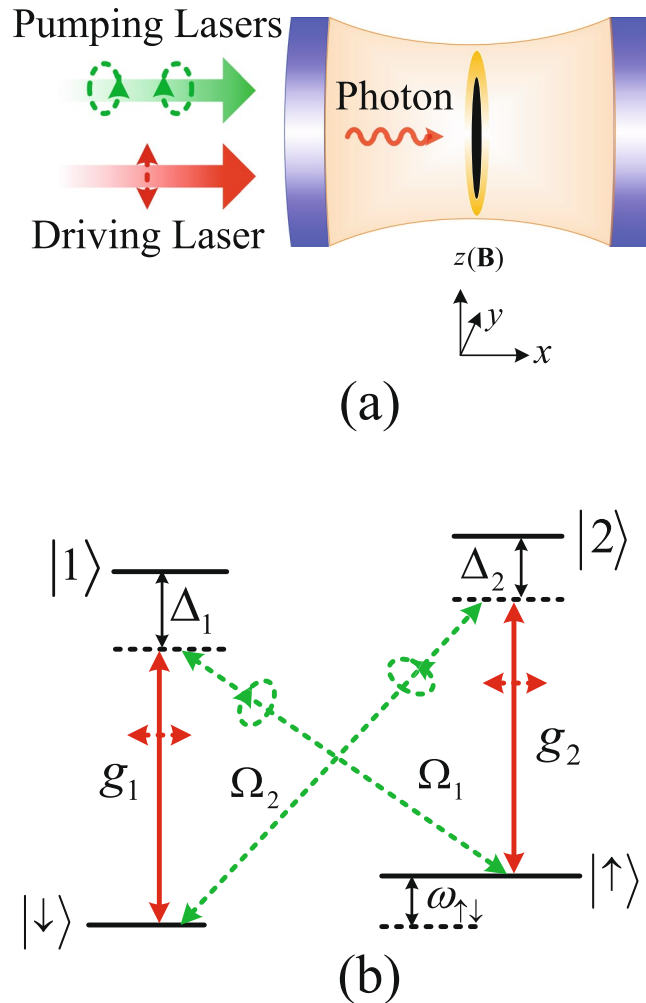


Figure 1. An ensemble of ultracold four-level fermions coupled to a high-finesse optical cavity. **(a)** Schematic of the proposed setup: the ultracold fermions (black online) are confined in a far-of-resonance optical trap (yellow online) in the yz plane along with a tightly-radial confinement in the x direction. The fermions are coupled to a high-finesse optical cavity, where the cavity mode is driven by a linearly polarized laser (with frequency ω_l) propagating along the x direction. Two transverse pumping lasers (with frequencies ω_A and ω_B), which are left- and right-handed circular polarized in the yz plane, propagate along the x direction. As a result, two Raman processes are induced. In order to obtain a time-independent Hamiltonian, the condition $\omega_l = (\omega_A + \omega_B)/2$ is required; see the detailed derivation in the main text. A magnetic field B is applied along the positive z direction, producing a Zeeman shift between two hyperfine ground states. **(b)** The atomic energy levels and their transitions. Each fermionic atom has two ground states ($|\uparrow\rangle$ and $|\downarrow\rangle$) and two excited states ($|1\rangle$ and $|2\rangle$). The $|\downarrow\rangle \leftrightarrow |1\rangle$ and $|\uparrow\rangle \leftrightarrow |2\rangle$ transitions (red solid lines) are caused by the quantized cavity field with fermion-photon coupling strengths g_1 and g_2 . The $|\uparrow\rangle \leftrightarrow |1\rangle$ and $|\downarrow\rangle \leftrightarrow |2\rangle$ transitions (green dashed lines) are governed by the transverse pumping lasers with Rabi frequencies Ω_1 and Ω_2 . $\omega_{\uparrow\downarrow} = \omega_{\uparrow} - \omega_{\downarrow}$ is the resonant frequency between the ground states $|\uparrow\rangle$ and $|\downarrow\rangle$ with eigenfrequencies ω_{\uparrow} and ω_{\downarrow} . Δ_1 and Δ_2 are the detuning from the excited states $|1\rangle$ and $|2\rangle$.

featuring two Fermi surfaces for the weak atomic resonant frequency. As such, the system exhibits a unique mixed phase where the normal and SR phases coexist. Finally, we discuss possible experiment observations of our results.

Results

Model and Hamiltonian. Motivated by the experiment with bosonic atoms⁵, we instead consider an ensemble of ultracold four-level fermions coupled to a high-finesse optical cavity; see Fig. 1. The fermions are confined in a far-off-resonance optical trap in the yz plane [see Fig. 1(a)], and their motion in the x direction is frozen, thus effectively realizing a 2D system. The cavity mode is driven by a linearly polarized laser, while the fermions are pumped by two transverse lasers which are left- and right-circular polarized in the yz plane, respectively. We consider fermionic atoms with four internal levels, which contain two degenerate ground states ($|\uparrow\rangle$ and $|\downarrow\rangle$) and two excited states ($|1\rangle$ and $|2\rangle$) [see Fig. 1(b)]. As clearly illustrated in Fig. 1, in our setup two Raman processes can be induced from the quantized cavity field and the two transverse pumping lasers.

The considered system can be effectively described by the following 2D Hamiltonian

$$\hat{H}_T(t) = \hat{H}_F + \hat{H}_P + \hat{H}_D(t) + \hat{H}_{AR}(t) + \hat{H}_{AP}, \quad (1)$$

where \hat{H}_F is the Hamiltonian for the free four-level fermions, i.e.,

$$\hat{H}_F = \sum_{i=1,2,\uparrow,\downarrow} \int d^2\mathbf{r} \hat{\psi}_i^\dagger(\mathbf{r}) \left(\frac{\hat{\mathbf{p}}^2}{2M} - \mu + \omega_i \right) \hat{\psi}_i(\mathbf{r}). \quad (2)$$

Here, $\hat{\psi}_i^\dagger(\mathbf{r})$ and $\hat{\psi}_i(\mathbf{r})$ ($i = 1, 2, \downarrow, \uparrow$) are the field operators for the fermionic atoms with mass M , μ is the chemical potential, and ω_i denotes the frequency of the i th eigenstate. The quantized cavity field and the driving laser are described by the Hamiltonian

$$\hat{H}_P + \hat{H}_D(t) = \omega_c \hat{a}^\dagger \hat{a} + \varepsilon (\hat{a} e^{i\omega t} + \hat{a}^\dagger e^{-i\omega t}), \quad (3)$$

where \hat{a}^\dagger (\hat{a}) creates (annihilates) the quantized cavity field with frequency ω_c , and ε (ω_l) labels the magnitude (frequency) of the driving laser. The Hamiltonian \hat{H}_{AR} represents the interaction between fermions and the transverse pumping lasers, which under the rotating-wave approximation can be written as

$$\hat{H}_{AR}(t) = \frac{1}{2} \int d^2\mathbf{r} [\Omega_1 \hat{\psi}_1^\dagger(\mathbf{r}) \hat{\psi}_\uparrow(\mathbf{r}) e^{-i\omega_A t} + \Omega_2 \hat{\psi}_2^\dagger(\mathbf{r}) \hat{\psi}_\downarrow(\mathbf{r}) e^{-i\omega_B t} + \text{H.c.}], \quad (4)$$

with Ω_1 and Ω_2 (ω_A and ω_B) being the Rabi frequencies (frequencies) of the two lasers. Finally, Hamiltonian \hat{H}_{AP} describes the interaction between fermions and the quantized cavity fields, i.e.,

$$\hat{H}_{AP} = \int d^2\mathbf{r} \left\{ [g_1 \hat{\psi}_1^\dagger(\mathbf{r}) \hat{\psi}_\downarrow(\mathbf{r}) + g_2 \hat{\psi}_2^\dagger(\mathbf{r}) \hat{\psi}_\uparrow(\mathbf{r})] \hat{a} + \text{H.c.} \right\}, \quad (5)$$

with g_1 and g_2 labeling the fermion-photon coupling strengths associated with the two pumping lasers, respectively.

It is more transparent to recast the time-dependent Hamiltonian (1) into a time-independent form. Introducing a unitary transformation $\hat{U}(t) = \exp(i\hat{H}t)$, where

$$\hat{H}' = \omega_l \hat{a}^\dagger \hat{a} + \frac{\omega_B}{2} [\hat{\psi}_2^\dagger(\mathbf{r}) \hat{\psi}_2(\mathbf{r}) - \hat{\psi}_\downarrow^\dagger(\mathbf{r}) \hat{\psi}_\downarrow(\mathbf{r})] + \frac{\omega_A}{2} [\hat{\psi}_1^\dagger(\mathbf{r}) \hat{\psi}_1(\mathbf{r}) - \hat{\psi}_\uparrow^\dagger(\mathbf{r}) \hat{\psi}_\uparrow(\mathbf{r})] \quad (6)$$

with $\omega_l = (\omega_B + \omega_A)/2$, we transform the Hamiltonian as $\hat{H}_1 = \hat{U}(t) \hat{H}_T(t) \hat{U}^\dagger(t) + i[\partial \hat{U}(t)/\partial t] \hat{U}^\dagger(t)$. Explicitly, we have

$$\begin{aligned} \hat{H}_1 = & \tilde{\omega} \hat{a}^\dagger \hat{a} + \varepsilon (\hat{a} + \hat{a}^\dagger) + \sum_{i=1,2,\uparrow,\downarrow} \int d^2\mathbf{r} \hat{\psi}_i^\dagger(\mathbf{r}) \left(\frac{\hat{\mathbf{p}}^2}{2M} - \mu \right) \hat{\psi}_i(\mathbf{r}) \\ & + \int d^2\mathbf{r} [\Delta_1 \hat{\psi}_1^\dagger(\mathbf{r}) \hat{\psi}_\uparrow(\mathbf{r}) + \Delta_2 \hat{\psi}_2^\dagger(\mathbf{r}) \hat{\psi}_2(\mathbf{r}) + \tilde{\omega}_\uparrow \hat{\psi}_\uparrow^\dagger(\mathbf{r}) \hat{\psi}_\uparrow(\mathbf{r}) + \tilde{\omega}_\downarrow \hat{\psi}_\downarrow^\dagger(\mathbf{r}) \hat{\psi}_\downarrow(\mathbf{r})] \\ & + \frac{1}{2} \int d^2\mathbf{r} [\Omega_1 \hat{\psi}_1^\dagger(\mathbf{r}) \hat{\psi}_\uparrow(\mathbf{r}) + \Omega_2 \hat{\psi}_2^\dagger(\mathbf{r}) \hat{\psi}_\downarrow(\mathbf{r}) + \text{H.c.}] \\ & + \int d^2\mathbf{r} \left\{ [g_1 \hat{\psi}_1^\dagger(\mathbf{r}) \hat{\psi}_\downarrow(\mathbf{r}) + g_2 \hat{\psi}_2^\dagger(\mathbf{r}) \hat{\psi}_\uparrow(\mathbf{r})] \hat{a} + \text{H.c.} \right\}. \end{aligned} \quad (7)$$

Here, $\tilde{\omega} = \omega_c - \omega_l$ is the effective cavity frequency, $\Delta_1 = \omega_1 - \omega_A/2$ ($\Delta_2 = \omega_2 - \omega_B/2$) denotes the detuning from the excited state $|1\rangle$ ($|2\rangle$), and $\tilde{\omega}_\uparrow = \omega_\uparrow + \omega_A/2$ ($\tilde{\omega}_\downarrow = \omega_\downarrow + \omega_B/2$) describes the effective frequency associated with the internal state $|\uparrow\rangle$ ($|\downarrow\rangle$).

To proceed, we recall that in the experiments³⁻⁵, a weak driving ($\varepsilon \rightarrow 0$) and large detuning ($|\Delta_{1,2}| \gg \{\Omega_{1,2}, g_{1,2}, \tilde{\omega}, \omega_0\}$) have been considered. Assuming similar scenarios here, this allows us to ignore the term $\varepsilon(\hat{a} + \hat{a}^\dagger)$ in the Hamiltonian (7), as well as adiabatically eliminate both excited states $|1\rangle$ and $|2\rangle$ ^{29,30}. This way, we obtain

$$\begin{aligned} \hat{H} = & \tilde{\omega} \hat{a}^\dagger \hat{a} + \sum_{\sigma=\uparrow,\downarrow} \int d^2\mathbf{r} \hat{\psi}_\sigma^\dagger(\mathbf{r}) \left(\frac{\hat{\mathbf{p}}^2}{2M} - \mu \right) \hat{\psi}_\sigma(\mathbf{r}) \\ & + \int d^2\mathbf{r} [\tilde{\omega}_\uparrow \hat{\psi}_\uparrow^\dagger(\mathbf{r}) \hat{\psi}_\uparrow(\mathbf{r}) + \tilde{\omega}_\downarrow \hat{\psi}_\downarrow^\dagger(\mathbf{r}) \hat{\psi}_\downarrow(\mathbf{r})] \\ & + \int d^2\mathbf{r} \left[\frac{|g_2|^2}{\Delta_2} \hat{\psi}_\uparrow^\dagger(\mathbf{r}) \hat{\psi}_\uparrow(\mathbf{r}) + \frac{|g_1|^2}{\Delta_1} \hat{\psi}_\downarrow^\dagger(\mathbf{r}) \hat{\psi}_\downarrow(\mathbf{r}) \right] \hat{a}^\dagger \hat{a} \\ & + \frac{1}{2} \int d^2\mathbf{r} \left\{ \left[\frac{g_2 \Omega_2^*}{\Delta_2} \hat{\psi}_\downarrow^\dagger(\mathbf{r}) \hat{\psi}_\uparrow(\mathbf{r}) + \frac{g_1 \Omega_1^*}{\Delta_1} \hat{\psi}_\uparrow^\dagger(\mathbf{r}) \hat{\psi}_\downarrow(\mathbf{r}) \right] \hat{a} + \text{H.c.} \right\}. \end{aligned} \quad (8)$$

Further considering

$$\frac{|g_1|^2}{\Delta_1} = \frac{|g_2|^2}{\Delta_2}, \quad \frac{g_1 \Omega_1^*}{\Delta_1} = \frac{g_2 \Omega_2^*}{\Delta_2}, \quad (9)$$

the Hamiltonian (8) can be simplified into

$$\begin{aligned} \hat{H} = & \omega \hat{a}^\dagger \hat{a} + \sum_{\sigma=\uparrow,\downarrow} \int d^2\mathbf{r} \hat{\psi}_\sigma^\dagger(\mathbf{r}) \left(\frac{\hat{\mathbf{p}}^2}{2M} - \mu \right) \hat{\psi}_\sigma(\mathbf{r}) - \omega_0 \int d^2\mathbf{r} [\hat{\psi}_\uparrow^\dagger(\mathbf{r}) \hat{\psi}_\uparrow(\mathbf{r}) - \hat{\psi}_\downarrow^\dagger(\mathbf{r}) \hat{\psi}_\downarrow(\mathbf{r})] \\ & + \frac{\eta}{\sqrt{N}} \int d^2\mathbf{r} [\hat{\psi}_\downarrow^\dagger(\mathbf{r}) \hat{\psi}_\uparrow(\mathbf{r}) + \hat{\psi}_\uparrow^\dagger(\mathbf{r}) \hat{\psi}_\downarrow(\mathbf{r})] (\hat{a} + \hat{a}^\dagger). \end{aligned} \quad (10)$$

Here, the factor $1/\sqrt{N}$, with N being the total atom number, is introduced so as to ensure a finite free energy per fermion in the thermodynamic limit^{9,10}. Furthermore, $\omega_0 = (\bar{\omega}_\uparrow - \bar{\omega}_\downarrow)/2$ is the effective resonant frequency between the ground states $|\uparrow\rangle$ and $|\downarrow\rangle$, which in Eq. (10) acts as an effective Zeeman field. Without loss of generality, below we shall take $\omega_0 > 0$. In addition, the parameter $\eta = \sqrt{N} g_1 \Omega_1^*/(2\Delta_1) = \sqrt{N} g_2 \Omega_2^*/(2\Delta_2)$ is the effective fermion-photon coupling strength, and $\omega = N\zeta + \bar{\omega}$ labels the atom-number dependent cavity frequency with $\zeta = |g_1|^2/\Delta_1 = |g_2|^2/\Delta_2$. We remark that all the parameter choice here are motivated by the experimental considerations³⁻⁵.

The Hamiltonian (10) represents the paradigmatic Fermi-Dicke model³¹ describing the fermion-photon interaction. We emphasize that our setup allows flexible controllability of all Hamiltonian parameters. For example, both ω_0 and ω can be tuned by modifying the frequencies of the driving laser and the transverse pumping lasers, while η can be controlled via the Rabi frequencies of the transverse pumping lasers.

Ground-state properties. Our goal is to investigate the ground state of the Hamiltonian (10). To this end, it is more convenient to transform to the momentum space representation. Writing

$$\hat{\psi}_\sigma(\mathbf{r}) = \frac{1}{\sqrt{S}} \sum_{\mathbf{k}, \sigma=\uparrow,\downarrow} \hat{C}_{\mathbf{k},\sigma} e^{i\mathbf{k}\cdot\mathbf{r}}, \quad (11)$$

where $\hat{C}_{\mathbf{k},\sigma}$ annihilates a fermion in the internal state σ with momentum \mathbf{k} and S is the system size (hereafter $S=1$ is set for convenience), we obtain

$$\begin{aligned} \hat{H} = & \omega \hat{a}^\dagger \hat{a} + \sum_{\mathbf{k}} \xi_{\mathbf{k}} \hat{C}_{\mathbf{k},\sigma}^\dagger \hat{C}_{\mathbf{k},\sigma} + \omega_0 \sum_{\mathbf{k}} (\hat{C}_{\mathbf{k},\uparrow}^\dagger \hat{C}_{\mathbf{k},\uparrow} - \hat{C}_{\mathbf{k},\downarrow}^\dagger \hat{C}_{\mathbf{k},\downarrow}) \\ & + \frac{\eta}{\sqrt{n}} \sum_{\mathbf{k}} (\hat{C}_{\mathbf{k},\uparrow}^\dagger \hat{C}_{\mathbf{k},\downarrow} + \hat{C}_{\mathbf{k},\downarrow}^\dagger \hat{C}_{\mathbf{k},\uparrow}) (\hat{a} + \hat{a}^\dagger). \end{aligned} \quad (12)$$

Here, $\xi_{\mathbf{k}} = \varepsilon_{\mathbf{k}} - \mu$, $\varepsilon_{\mathbf{k}} = \mathbf{k}^2/2M$ is the kinetic energy, and $n = K_F^2/(2\pi) = E_F M/\pi$ is the 2D density of fermions with $E_F = K_F^2/(2M)$ being the Fermi energy and K_F being the Fermi momentum.

In solving the ground state of the Hamiltonian (12), we will rely on the mean-field approximation, i.e., by replacing \hat{a} with its steady-state value. Specifically, we write down the Heisenberg-Langevin equation for the cavity field operator \hat{a} ^{32,33}, taking into account of the cavity decay with rate κ , i.e.,

$$i \frac{\partial \hat{a}}{\partial t} = [\hat{a}, \hat{H}] - i\kappa \hat{a} + \hat{\gamma}_{\text{in}}(t). \quad (13)$$

For the quantum noise operator $\hat{\gamma}_{\text{in}}(t)$, we have $\langle \hat{\gamma}_{\text{in}}^\dagger(t) \hat{\gamma}_{\text{in}}(t') \rangle = 2\kappa \delta(t - t')$ and $\langle \hat{\gamma}_{\text{in}}(t) \hat{\gamma}_{\text{in}}^\dagger(t') \rangle = 0$. Since quantum noise usually occurs on a much shorter time scale than $1/\kappa$ ³⁴, its average effect can be generically ignored on the time scale relevant for the steady state. When $1/\kappa$ is much shorter than the time scales of system dynamics, a steady-state solution^{3,35} to Eq. (13) can be found, i.e.,

$$\alpha = \langle \hat{a} \rangle = \frac{\eta \sum_{\mathbf{k}} \langle \hat{C}_{\mathbf{k},\uparrow}^\dagger \hat{C}_{\mathbf{k},\downarrow} + \hat{C}_{\mathbf{k},\downarrow}^\dagger \hat{C}_{\mathbf{k},\uparrow} \rangle}{\sqrt{n}(-\omega + i\kappa)}. \quad (14)$$

Motivated by the experiments^{3,4} which shows that the mean-photon number $\langle \hat{a}^\dagger \hat{a} \rangle = |\alpha|^2$ determines the SR properties, we henceforth refer to it as the SR order parameter.

By approximating $\hat{a} \approx \langle \hat{a} \rangle$ in Eq. (12) using Eq. (14), we obtain a quadratic Hamiltonian

$$\hat{H} = \sum_{\mathbf{k}} \hat{\Psi}_{\mathbf{k}}^\dagger M_{\mathbf{k}} \hat{\Psi}_{\mathbf{k}} + \omega |\alpha|^2. \quad (15)$$

Here, $\hat{\Psi}_{\mathbf{k}} = (\hat{C}_{\mathbf{k},\uparrow}, \hat{C}_{\mathbf{k},\downarrow})^T$ is the standard Nambu spinor, and $M_{\mathbf{k}}$ is the photon-number dependent BdG matrix, i.e.,

$$M_{\mathbf{k}} = \begin{pmatrix} \xi_{\mathbf{k}} - \omega_0 & \bar{\eta} \\ \bar{\eta} & \xi_{\mathbf{k}} + \omega_0 \end{pmatrix}, \quad (16)$$

with $\bar{\eta} = \eta(\alpha + \alpha^*)/\sqrt{n}$. Now, the Hamiltonian (15) can be easily diagonalized as

$$\hat{H} = \sum_{\mathbf{k}} (E_{\mathbf{k},+} \hat{\alpha}_{\mathbf{k},+}^\dagger \hat{\alpha}_{\mathbf{k},+} + E_{\mathbf{k},-} \hat{\alpha}_{\mathbf{k},-}^\dagger \hat{\alpha}_{\mathbf{k},-}) + \omega |\alpha|^2, \tag{17}$$

where $\hat{\alpha}_{\mathbf{k},\pm}$ describe the fermionic Bogoliubov quasiparticles, whose energy is given by

$$E_{\mathbf{k},\pm} = \xi_{\mathbf{k}} \pm \sqrt{\bar{\eta}^2 + \omega_0^2}, \tag{18}$$

with $\bar{\eta}^2 = 4\omega^2\eta^2 |\alpha|^2 / [n(\omega^2 + \kappa^2)]$. Note that $E_{\mathbf{k},\pm}$ can be either positive or negative depending on parameter choices. Regrouping terms with positive and negative energies using the Heaviside step function $\Theta(x)$, we recast Eq. (17) as

$$\hat{H} = \sum_{\mathbf{k},\pm} E_{\mathbf{k},\pm} \Theta(E_{\mathbf{k},\pm}) \hat{\alpha}_{\mathbf{k},\pm}^\dagger \hat{\alpha}_{\mathbf{k},\pm} - \sum_{\mathbf{k},\pm} E_{\mathbf{k},\pm} \Theta(-E_{\mathbf{k},\pm}) \hat{\alpha}_{\mathbf{k},\pm}^\dagger \hat{\alpha}_{\mathbf{k},\pm} + E_G, \tag{19}$$

where E_G is the ground-state energy expressed by

$$E_G = \sum_{\mathbf{k}} E_{\mathbf{k},+} \Theta(-E_{\mathbf{k},+}) + E_{\mathbf{k},-} \Theta(-E_{\mathbf{k},-}) + \omega |\alpha|^2. \tag{20}$$

Despite the formal expression of the ground-state energy, Eq. (20) contains two variables, i.e., μ and $|\alpha|$, which are to be determined from the particle number equation $\partial E_G / \partial \mu = -n$ and the SR equation $\partial E_G / \partial (|\alpha|) = 0$. Explicitly, we have

$$\sum_{\mathbf{k}} (-1) [f(-E_{\mathbf{k},+}) + f(-E_{\mathbf{k},-})] = n, \tag{21}$$

$$|\alpha| \left\{ \sum_{\mathbf{k}} -2\omega\eta^2 [f(-E_{\mathbf{k},-}) - f(-E_{\mathbf{k},+})] + n\bar{\chi}(\omega^2 + \kappa^2) \right\} = 0, \tag{22}$$

where $f(-E_{\mathbf{k},\pm}) = \Theta(-E_{\mathbf{k},\pm}) - E_{\mathbf{k},\pm} \delta(-E_{\mathbf{k},\pm})$ and $\bar{\chi} = \sqrt{\bar{\eta}^2 + \omega_0^2}$. In deriving Eqs (21) and (22), we have used the identity $\Theta'(x) = \delta(x)$ with $\delta(x)$ being the delta function.

Equations (20–22) allow complete specification of the ground state: The ground-state energy can be obtained in a *self-consistent* manner by solving Eqs (21) and (22) for a fixed atom density n . It is important to bear in mind that solutions of above equations must be supplemented with a careful stability analysis, which we describe below.

Phase diagram. We now detail our analysis on the ground-state properties. We shall be interested in four quantities: the ground-state energy per fermion $\bar{E}_G = E_G/n$, the chemical potential μ , the scaled mean-photon number $|\bar{\alpha}|^2$, and the scaled polarization³⁶ measuring the response to the effective Zeeman field defined by

$$\bar{m} = \frac{n_\uparrow - n_\downarrow}{n} = -\frac{\partial \bar{E}_G}{\partial \omega_0}. \tag{23}$$

As we shall see, their ground-state values depend crucially on the strength of the effective Zeeman field ω_0 and the effective fermion-photon coupling strength η , in particular, new features compared to their boson counterpart are found in the regime $\omega_0 < E_F$. Note that all energies will be measured in units of E_F hereupon.

In order to gain some intuition, let us first consider the simplest case $\eta=0$ corresponding to a free Fermi gas. Transforming Eq. (20) into an integral over momenta as usual, we calculate the ground-state energy per fermion as

$$\bar{E}_G = -\frac{1}{4E_F} [(\mu + \omega_0)^2 \Theta(\mu + \omega_0) + (\mu - \omega_0)^2 \Theta(\mu - \omega_0)]. \tag{24}$$

Because $\mu + \omega_0 < 0$ will entail a unphysical result $\bar{E}_G = 0$ which excludes existence of real fermions^{37,38}, we shall limit our subsequent discussions in the regime $\mu + \omega_0 > 0$. There, the Fermi gas can exhibit different ground states depending on whether $\omega_0 > \mu$ or $\omega_0 < \mu$.

When $\omega_0 > \mu$, $\Theta(\mu - \omega_0) = 0$ and Eq. (24) becomes

$$\bar{E}_G = -\frac{(\omega_0 + \mu)^2}{4E_F}. \tag{25}$$

Based on Eqs (21), (23) and (25), we obtain

$$\bar{E}_G = -E_F, \quad \mu = 2E_F - \omega_0, \quad \bar{m} = 1. \tag{26}$$

Thus the Fermi gas is in a normal phase characterized by a full polarization and one Fermi surface with $\mu_\uparrow = 2E_F$, and we shall refer to it as the N-I phase.

In contrast, when $\omega_0 < \mu$, $\Theta(\mu - \omega_0) = 1$ and Eq. (24) becomes

$$\bar{E}_G = -\frac{\omega_0^2 + \mu^2}{4E_F}. \quad (27)$$

Based on Eqs (21), (23) and (25), we have

$$\bar{E}_G = -\frac{(E_F^2 + \omega_0^2)}{2E_F}, \quad \mu = E_F, \quad \bar{m} = \frac{\omega_0}{E_F}. \quad (28)$$

Hence the Fermi gas is only partially polarized and exhibits two Fermi surfaces, i.e., $\mu_+ = E_F + \omega_0$ and $\mu_- = E_F - \omega_0$. We shall call it as the N-II phase. It is clear from Eqs (26) and (28) that, by tuning the parameter ω_0 across the critical point $\omega_0^c = E_F$ ³⁷, the Fermi gas undergoes a first-order transition between the N-I to N-II phases.

Now, suppose there exists a weak effective coupling between the photon and fermions, i.e., η is small. Still, the noninteracting terms in the Hamiltonian (12) dominate the system dynamics, such that $|\alpha|^2 = 0$ is expected to persist for the ground state and the Fermi gas remains in the N-I or N-II phase (depending on values of ω_0).

However, the ground-state properties of the Fermi gas can change drastically from both normal phases for a strong photon-fermion coupling when η is increased above a threshold. As we show now, when the interaction part of the Hamiltonian (12) dominates, the system can acquire a macroscopic collective excitation with $|\alpha|^2 \neq 0$, i.e., a quantum phase transition into the SR phase occurs when η is above some critical values. Integrating Eq. (20) over the momenta, we obtain

$$\bar{E}_G = -\frac{1}{4E_F}[\mu_+^2 + \mu_-^2 \Theta(\mu_-)] + \omega |\bar{\alpha}|^2, \quad (29)$$

with $\mu_{\pm} = \mu \pm \bar{\chi}$ and $|\bar{\alpha}|^2 = |\alpha|^2/n$ being the scaled mean-photon number. We next analyze Eq. (29) when (i) $\mu_- < 0$ and (ii) $\mu_- \geq 0$.

Consider first the case $\mu_- < 0$, where Eq. (29) becomes

$$\bar{E}_G = -\frac{1}{4E_F}\mu_+^2 + \omega |\bar{\alpha}|^2, \quad (30)$$

and Eqs (21–23) take the following form

$$\mu + \sqrt{\eta^2 + \omega_0^2} = 2E_F, \quad (31)$$

$$|\bar{\alpha}| \left[2\omega - \frac{2\omega^2 \eta^2 (\mu + \sqrt{\eta^2 + \omega_0^2})}{E_F(\omega^2 + \kappa^2) \sqrt{\eta^2 + \omega_0^2}} \right] = 0, \quad (32)$$

$$\frac{\omega_0(\mu + \sqrt{\eta^2 + \omega_0^2})}{2E_F \sqrt{\eta^2 + \omega_0^2}} = \bar{m}. \quad (33)$$

We can obtain two set of solutions, namely,

$$\mu = 2E_F - \omega_0, \quad |\bar{\alpha}| = 0, \quad \bar{m} = 1, \quad (34)$$

or

$$\mu = 2 \left(E_F - \frac{\omega \eta^2}{\omega^2 + \kappa^2} \right), \quad |\bar{\alpha}| = \sqrt{\frac{\eta^2}{\omega^2 + \kappa^2} - \frac{\omega_0^2(\omega^2 + \kappa^2)}{4\omega^2 \eta^2}}, \quad \bar{m} = \frac{\omega_0(\omega^2 + \kappa^2)}{2\omega \eta^2}. \quad (35)$$

Obviously, while solutions (34) are associated with the normal phase, solutions (35) exhibit SR property. Furthermore, as mentioned earlier, the ground-state solutions must satisfy the stability condition as defined by $\partial^2 \bar{E}_G / \partial (|\bar{\alpha}|)^2 > 0$. Consequently, we find that the stability condition for the normal solution [see Eq. (34)] is $\eta < \eta_c^{(1)}$ with

$$\eta_c^{(1)} = \sqrt{\frac{\omega_0(\omega^2 + \kappa^2)}{2\omega}}. \quad (36)$$

Instead, the SR solution [see Eq. (35)] is only stable when $\eta > \eta_c^{(1)}$. Notice that since $\mu_- = \mu - \bar{\chi} < 0$, this additionally requires $\eta > \eta_c^{(2)}$ with

$$\eta_c^{(2)} = \sqrt{\frac{E_F(\omega^2 + \kappa^2)}{2\omega}}. \quad (37)$$

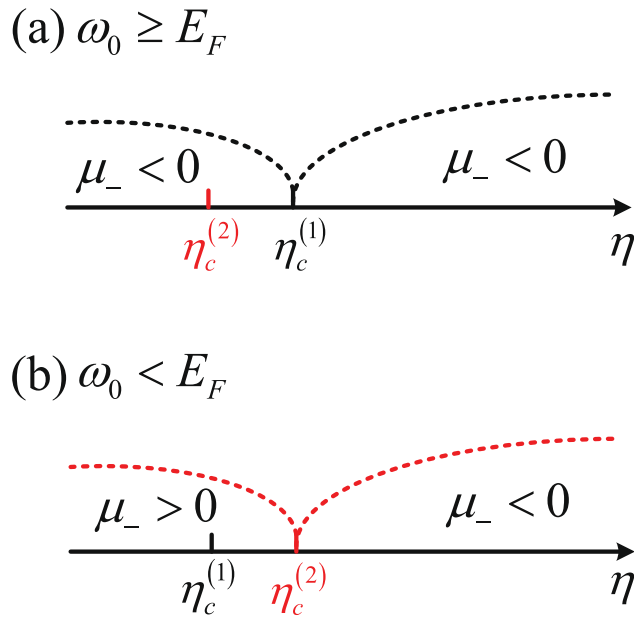


Figure 2. Comparison of the critical points $\eta_c^{(1)}$ and $\eta_c^{(2)}$ for (a) $\omega_0 \geq E_F$ and (b) $\omega_0 < E_F$. When $\omega_0 \geq E_F$, $\eta_c^{(1)} > \eta_c^{(2)}$, and $\mu_- < 0$ for both $0 < \eta < \eta_c^{(1)}$ and $\eta > \eta_c^{(1)}$. When $\omega_0 < E_F$, $\eta_c^{(1)} < \eta_c^{(2)}$, and $\mu_- < 0$ for $\eta > \eta_c^{(2)}$ and $\mu_- > 0$ for $0 < \eta < \eta_c^{(2)}$.

Following from above analysis, we find that for $\omega_0 \geq E_F$ [c.f. Fig. 2(a)] and thereby $\eta_c^{(1)} > \eta_c^{(2)}$, the ground state of the Fermi gas is in the N-I phase for $0 < \eta < \eta_c^{(1)}$, but transits into the SR phase for $\eta > \eta_c^{(1)}$; see summarized results below

$$\bar{E}_G = \begin{cases} -E_F & 0 < \eta < \eta_c^{(1)} \\ -E_F + \frac{\omega\eta^2}{\omega^2 + \kappa^2} - \frac{\omega_0^2(\omega^2 + \kappa^2)}{4\omega\eta^2} & \eta > \eta_c^{(1)} \end{cases}, \quad (38)$$

with corresponding relevant quantities given by

$$\mu = \begin{cases} 2E_F - \omega_0 & 0 < \eta < \eta_c^{(1)} \\ 2(E_F - \frac{\omega\eta^2}{\omega^2 + \kappa^2}) & \eta > \eta_c^{(1)} \end{cases}, \quad (39)$$

$$|\bar{\alpha}| = \begin{cases} 0 & 0 < \eta < \eta_c^{(1)} \\ \sqrt{\frac{\eta^2}{\omega^2 + \kappa^2} - \frac{\omega_0^2(\omega^2 + \kappa^2)}{4\omega^2\eta^2}} & \eta > \eta_c^{(1)} \end{cases}, \quad (40)$$

$$\bar{m} = \begin{cases} 1 & 0 < \eta < \eta_c^{(1)} \\ \frac{\omega_0(\omega^2 + \kappa^2)}{2\omega\eta^2} & \eta > \eta_c^{(1)} \end{cases}. \quad (41)$$

The ground-state properties described by Eqs (38)–(41) exhibit two features. First, the quantum phase transition between the N-I and SR phases is second order in nature: while the first-order derivative of \bar{E}_G is continuous with respect to η , its second order derivative develops discontinuity at the critical point $\eta_c^{(1)}$, as in the case with ultracold Bose atoms^{9,10}. Second, in contrast to the N-I phase, the SR phase features macroscopic collective excitations for both fermions and photons, i.e., we have both $|\bar{\alpha}| \neq 0$ and $\bar{m} \neq 0$. Also note that while $\bar{m} \sim \eta^2$, we see $\mu \sim \eta^{-2}$. These analytical results are confirmed by our numerical calculations as illustrated by Fig. 3, where we plot \bar{E}_G , μ , $|\bar{\alpha}|^2$, and \bar{m} as functions of η , respectively.

Next, turning to the case $\mu_- = \mu - \bar{\chi} \geq 0$, we find from Eq. (29) that

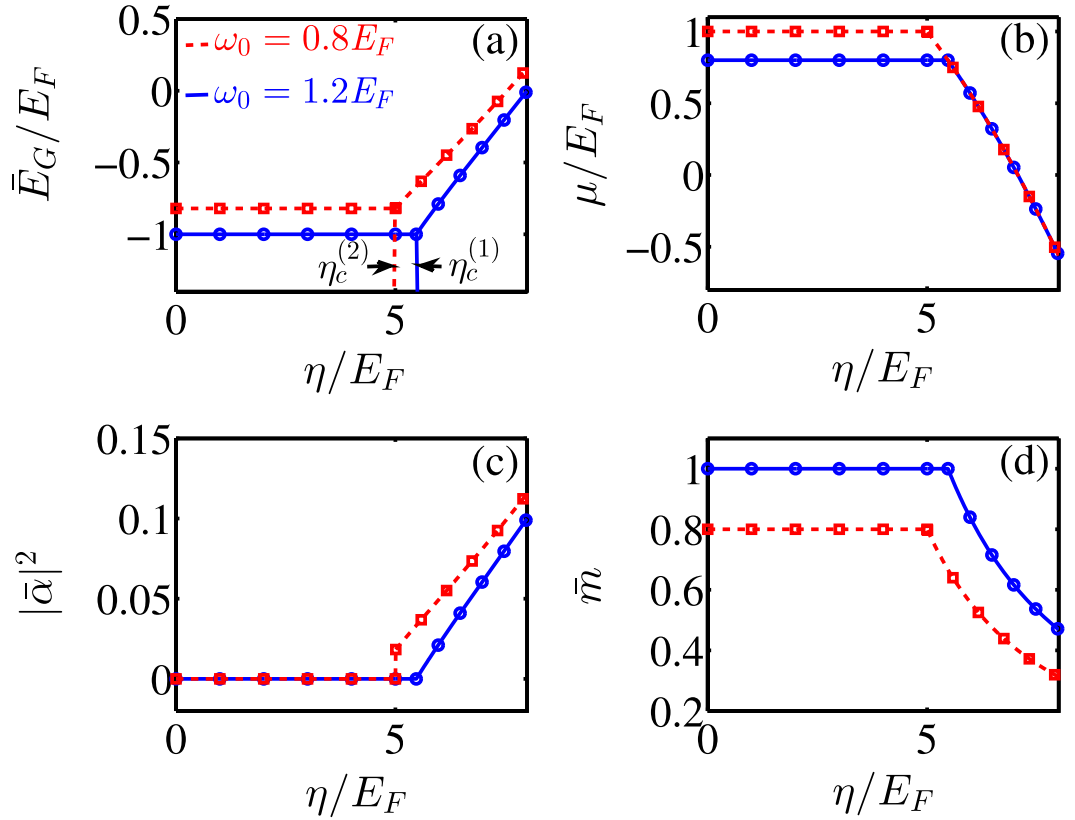


Figure 3. (a) The scaled ground-state energy \bar{E}_G/E_F , (b) the chemical potential μ/E_F , (c) the scaled mean-photon number $|\bar{\alpha}|^2$, and (d) the scaled polarization \bar{m} as functions of the effective atom-photon coupling strength η/E_F . Analytical results are depicted by blue-solid and red-dashed lines, while the open symbols represent numerical simulations. For the atom-number dependent cavity frequency, we choose $\omega = 10E_F$, and we take the cavity decay rate as $\kappa = 20E_F$. For $\omega_0 = 1.2E_F$, we take $\eta_c^{(1)} = 5.48E_F$, and when $\omega_0 = 0.8E_F$, we take $\eta_c^{(2)} = 5E_F$.

$$\bar{E}_G = -\frac{1}{4E_F}(\mu_+^2 + \mu_-^2) + \omega|\bar{\alpha}|^2. \tag{42}$$

Imposing the stability condition $\partial^2\bar{E}_G/\partial(|\bar{\alpha}|^2) > 0$, and keeping in mind $\mu_- \geq 0$, we find that in the regimes $\omega_0 < E_F$ and $0 < \eta < \eta_c^{(2)}$, the relevant ground-state solutions are

$$\mu = E_F, |\bar{\alpha}| = 0, \bar{m} = \frac{\omega_0}{E_F}. \tag{43}$$

Note that for $\omega_0 < E_F$ and $\eta > \eta_c^{(2)}$, we would have $\mu_- < 0$ [c.f. Fig. 2(b)], where the ground-state solutions are of the form of Eq. (35). Thus in contrast to the case $\omega_0 \geq E_F$, the ground state of the Fermi gas with $\omega_0 < E_F$ exhibits the N-II phase for $0 < \eta < \eta_c^{(2)}$ and the SR phase for $\eta > \eta_c^{(2)}$. We summarize results below

$$\bar{E}_G = \begin{cases} -\frac{E_F}{2} - \frac{\omega_0^2}{2E_F} & 0 < \eta < \eta_c^{(2)} \\ -E_F + \frac{\omega\eta^2}{\omega^2 + \kappa^2} - \frac{\omega_0^2(\omega^2 + \kappa^2)}{4\omega\eta^2} & \eta > \eta_c^{(2)} \end{cases}. \tag{44}$$

We see that a quantum phase transition from the N-II phase to the SR phase occurs at the critical point $\eta_c^{(2)}$, which is first order in nature and is accompanied by a sudden change in $|\bar{\alpha}|^2$ [see also red-dashed curves in Fig. 3(c)].

Interestingly, at the critical regime $\eta = \eta_c^{(2)}$, the scaled ground-state energies of the N-II and SR phases become equal, meaning both phases coexist. We shall therefore call it *the N-II-SR mixed phase*. In order to characterize this mixed phase, let x_0 stand for the fraction of the N-II part in the mixed phase, which can take arbitrary value in the regime $0 \leq x_0 \leq 1$. We find (see Methods Section for detailed derivation)

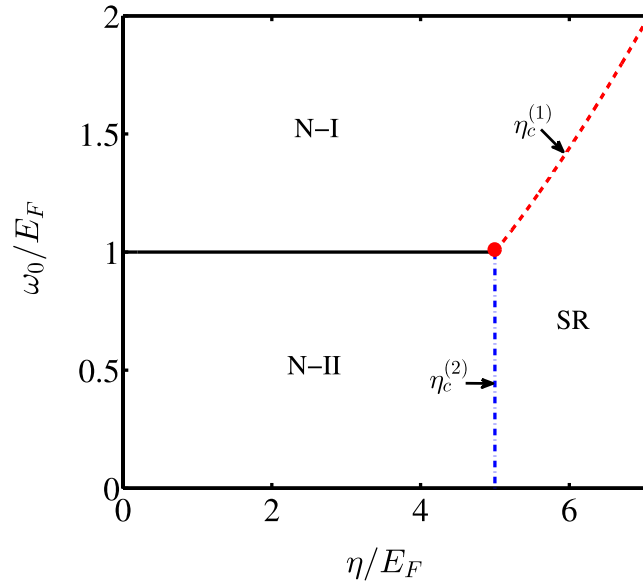


Figure 4. Phase diagram as a function of the effective resonant frequency ω_0/E_F and the effective fermion-photon coupling strength η/E_F . The atom-number dependent cavity frequency ω and the cavity decay rate κ are the same as those in Fig. 3. When the effective resonant frequency is chosen as $\omega_0 = E_F, \eta_c^{(1)} = \eta_c^{(2)}$.

$$\bar{E}_G = \mu - \frac{x_0(\omega_0^2 + E_F^2)}{2E_F} - \frac{(1 - x_0)}{2}(E_F + \frac{\omega_0^2}{E_F}), \tag{45}$$

$$\mu = E_F, \tag{46}$$

$$|\bar{\alpha}| = \sqrt{\frac{E_F^2 - \omega_0^2}{2\omega E_F}}, \tag{47}$$

$$\bar{m} = \frac{x_0\omega_0}{E_F} + (1 - x_0)\frac{\omega_0(\omega^2 + \kappa^2)}{2\omega\eta^2}. \tag{48}$$

Since both the SR and N-II phases exhibit $\bar{m} \neq 0$ [see Eqs (35) and (28)], the former due to the macroscopic collective excitation of fermions while the later induced by the effective Zeeman field, it is naturally expected that both mechanisms contribute to the nonzero polarization of the N-II-SR mixed phase [see Eq. (48)]. In addition, we find two first-order quantum phase transitions, from the N-II-SR phase to the N-II phase and to the SR phase, respectively. This is different from the boson counterpart, as well as the previously discussed N-I phase, where the corresponding transitions are second order^{9,10}.

Collecting all above results, we plot in Fig. 4 the phase diagram in the entire parameter regimes of ω_0/E_F and η/E_F . As predicted previously, while the quantum phase transition from the N-I phase to the SR phase is second order, a first-order transition occurs between the N-II and SR phases due to coexistence of both phases at the critical line. In addition, the phase diagram exhibits a tri-critical point (see the red dotted curves), where the quantum phase transition changes its character from the first to the second order.

Parameter estimation and possible experimental observation. We now provide an estimation of the relevant parameters taking ⁴⁰K atom as the example. For the fermionic ⁴⁰K atoms with the Fermi energy $E_F \sim 0.73$ MHz, the ground states with ²S_{1/2} are represented by $|\uparrow\rangle = |F = 9/2, m_F = 9/2\rangle$ and $|\downarrow\rangle = |F = 9/2, m_F = 7/2\rangle$. For the excited states with ²P_{1/2}, we choose $|1\rangle = |F = 9/2, m_F = 7/2\rangle$ and $|2\rangle = |F = 9/2, m_F = 9/2\rangle$, with F and m_F labeling the total angular momentum and magnetic quantum numbers, respectively.

Considering the optical properties of the ⁴⁰K D1-line, we take the cavity length as 178 μm and the wavelengths of the transverse pumping lasers as 770 nm. This ensures that both g_1 and g_2 characterizing the fermion-photon coupling strength are at the order of MHz, such that the rotating-wave approximation leading to Eqs (4) and (5) is valid. For a cavity with a waist radius 27 μm and a finesse $\sim 10^5$, we estimate its decay rate κ is at the order of MHz. For the effective fermion-photon coupling strength $\eta = \sqrt{N}g_1\Omega_1^*/(2\Delta_1) = \sqrt{N}g_2\Omega_2^*/(2\Delta_2)$, thanks to the prefactor \sqrt{N} , a magnitude of MHz can be achieved simply by modifications of the Rabi frequencies of the transverse pumping lasers, despite the large detuning required by the adiabatic approximation leading to Eq. (8).

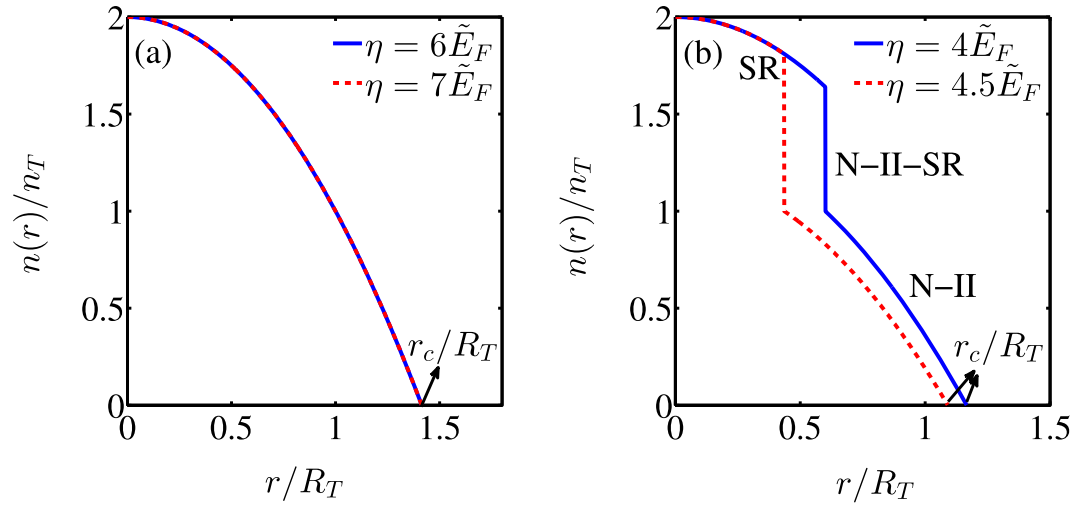


Figure 5. The density distributions $n(r)/n_0$ for (a) $\omega_0 \geq \tilde{E}_F$ and (b) $\omega_0 < \tilde{E}_F$ along the radial direction r/R_T . The atom-number dependent cavity frequency ω and the cavity decay rate κ are the same as those in Fig. 3. The scaled polarization is taken as $\bar{m} = 0.5$.

Finally, the effective resonant frequency $\omega_0 = (\tilde{\omega}_\perp - \tilde{\omega}_\parallel)/2$ and the atom-number dependent cavity frequency $\omega = N\zeta + \tilde{\omega}$ can be easily controlled by tuning the frequencies of the driving and transverse pumping lasers. In the experiments³, both ω_0 and ω can be tuned from $-\text{GHz}$ to GHz and even beyond.

We conclude this section by briefly discussing how to probe the predicted quantum phases and phase diagrams. As has been elaborated, the physics of the ground-state phases is determined by the scaled mean-photon number $|\bar{\alpha}|^2$ and the scaled polarization \bar{m} . Building on the development of the state of the art experimental techniques, \bar{m} can be measured by observing the different density distributions between the two-component Fermi gas^{39,40}, while α can be detected using the calibrated single-photon counting modules which allows for the *in situ* monitor of the intra-cavity light intensity³. We thus expect that our results to be feasible within the experimental capabilities.

Discussion

In realistic experiments, there typically exists a shallow harmonic external confining potential, which can be modeled by $V(r) = \omega_\perp^2 r^2/2$, where ω_\perp is the harmonic trap frequency and r is the harmonic trap radius. In order to estimate its effect, we first use the local density approximation⁴¹ to obtain an effective chemical potential $\mu(r) = \mu_0 - V(r)$, where μ_0 is the chemical potential at the center of the harmonic trap and $\mu(r)$ determines the total density $n = n_\uparrow + n_\downarrow$. Then, the density distribution $n(r)$ and the magnetization distribution $m(r)$ can be solved from⁴²

$$N = 2\pi \int r dr n(r), \quad \bar{m} = \frac{2\pi}{N} \int r dr m(r). \tag{49}$$

In Fig. 5, we plot the density distributions $n(r)/n_0$ in the radial direction for (a) $\omega_0 \geq \tilde{E}_F$ and (b) $\omega_0 < \tilde{E}_F$, respectively, where $n_0 = M\tilde{E}_F/(2\pi)$, $R_T = \sqrt{2\tilde{E}_F}/\omega_\perp$ is the Thomas-Fermi radius, and $\tilde{E}_F = \sqrt{N}\hbar\omega_\perp$ is the Fermi energy in the trapped systems. As shown in Fig. 5(a), for $\omega_0 \geq \tilde{E}_F$ (fully polarized fermions), the density profile does not depend on the effective fermion-photon coupling strength η , which implies that the critical line $\eta = \eta_c^{(1)}$ for the second-order quantum phase transition from the N-I phase to the SR phase is unaffected by the trapping potential. However, for $\omega_0 < \tilde{E}_F$ (partially polarized fermions), the density profile depends strongly on the effective fermion-photon coupling strength η , leading to the modification of the critical line for the first-order quantum phase transition from the N-II phase to the SR phase, as shown in Fig. 5(b). Moreover, the predicted N-II-SR mixed phase only exists near the center of the trap and the corresponding density profile has thus a jump discontinuity, which provides an experimentally observable signature. We also note that the presence of the harmonic trap renders the system to become of finite size, i.e., the density profile vanishes for size $r/R_T > r_c/R_T$, where r_c denotes the size of the trap, as shown in both Fig. 5(a) and 5(b).

In addition, when the decay rate κ , which has the order of MHz in experiments, is much larger than the external atomic degrees of freedom, the relatively slow atoms at times $t \gg 1/\kappa$ feel an average affect of steady-state photons, i.e., Eq. (14). Furthermore, when the system enters the SR phase with a large mean-photon number, the commutator $[\hat{a}, \hat{a}^\dagger] = 1$ can be ignored at the leading order results. Thus, it is reasonable to neglect the non-commutability between \hat{a} and \hat{a}^\dagger and just set them to their steady-state averaged value^{3,4,12-25}. Based on the above two arguments, the employed mean-field approximation, which assumes to approximate the photon annihilation operator by its steady-state averaged value, provides a good description of the system within our context.

In summary, we have analytically investigated the ground-state properties of a 2D polarized degenerate Fermi gas coupled to a high-finesse optical cavity. By solving the photon-number dependent BdG equation, we have found rich quantum phases and phase diagrams, which depend crucially on the fermion-photon coupling strength and the atomic resonant frequency (effective Zeeman field). In particular, for the weak atomic resonant frequency, we have shown that there exists a mixed phase where the N-II and SR phases coexist. In addition, we have revealed a first-order quantum phase transition from the N-II phase to the SR phase, which contrasts to the familiar second-order transition for the case with bosons. Finally, we have presented a parameter estimation and have addressed briefly how to detect these predicted quantum phases and phase diagrams in experiments.

Methods

In this Section, we present a detailed derivation of Eqs (45)–(48). We denote by $\mu_{N-II-SR} \in [\mu_{N-II}, \mu_{SR}]$ the chemical potential in the N-II-SR mixed phase, and let n_{N-II} (n_{SR}) and μ_{N-II} (μ_{SR}) denote the atom density and the chemical potential in the N-II (SR) phase, respectively. In terms of the fraction $0 \leq x_0 \leq 1$ of the N-II phase, we have⁴²

$$n = x_0 n_{N-II}(\mu_{N-II-SR}, \omega_0) + (1 - x_0) n_{SR}(\mu_{N-II-SR}, \omega_0, \eta). \quad (50)$$

When $x_0 = 1$, we simply have the N-II phase [see Eq. (28)], and $n_{N-II} = M\mu_{N-II}/\pi$. Instead, when $x_0 = 0$, $\bar{E}_G^{SR}(\mu_{SR}, \omega_0, \eta)$, μ_{SR} , $|\bar{\alpha}|_{SR}$, n_{SR} , and \bar{m}_{SR} are given by

$$\bar{E}_G^{SR} = -\frac{\mu_{SR}^2}{4E_F A} - \frac{\omega_0^2(\omega^2 + \kappa^2)}{4\omega\eta^2}, \quad (51)$$

$$\mu_{SR} = 2\left(E_F - \frac{\omega\eta^2}{\omega^2 + \kappa^2}\right), \quad (52)$$

$$|\bar{\alpha}|_{SR} = \frac{1}{2} \sqrt{\frac{\mu_{SR}^2 \eta^2}{(\omega^2 + \kappa^2) E_F^2 A^2} - \frac{\omega_0^2(\omega^2 + \kappa^2)}{\omega^2 \eta^2}}, \quad (53)$$

$$n_{SR} = \frac{M\mu_{SR}}{2\pi A}, \quad (54)$$

$$\bar{m}_{SR} = \frac{\omega_0(\omega^2 + \kappa^2)}{4\omega\eta^2}, \quad (55)$$

where $A = 1 - \omega\eta^2/[E_F(\omega^2 + \kappa^2)]$.

Using the phase equilibrium condition $\bar{E}_G^{N-II}(\mu_{N-II-SR}, \omega_0) = \bar{E}_G^{SR}(\mu_{N-II-SR}, \omega_0, \eta)$ ^{37, 42}, together with Eqs (28) and (51), we see that when $\mu_{N-II-SR} = \mu_{N-II} = E_F$ corresponding to $x_0 = 1$, the phase boundary between the N-II phase and the N-II-SR mixed phase is described by $\eta = \eta_c^{(2)}$. On the other hand, when $\mu_{N-II-SR} = \mu_{SR} = 2E_F - 2\omega\eta^2/(\omega^2 + \kappa^2)$ corresponding to $x_0 = 0$, the phase boundary between the N-II-SR mixed phase and the SR phase is also described by $\eta = \eta_c^{(2)}$. In addition, for the N-II-SR mixed phase, we can determine $\mu_{N-II-SR}$ from the relation $\bar{E}_G^{N-II}(\mu_{N-II-SR}, \omega_0) = \bar{E}_G^{SR}(\mu_{N-II-SR}, \omega_0, \eta)$, which gives

$$\mu_{N-II-SR} = E_F. \quad (56)$$

This is the same as Eq. (46). Substituting Eq. (56), n_{N-II} , and n_{SR} into Eq. (50), we find x_0 can take arbitrary values ranging from 0 to 1.

Finally, let us prove that the ground state of the N-II-SR mixed phase is stable. Due to the existence of both N-II and SR phases, the scaled ground-state energy in this mixed phase is defined by^{37, 42}

$$\begin{aligned} \bar{E}_G^{N-II-SR}(\omega_0, \eta) &= \mu_{N-II-SR} + x_0 \bar{E}_G^{N-II}(\mu_{N-II-SR}, \omega_0) \\ &+ (1 - x_0) \bar{E}_G^{SR}(\mu_{N-II-SR}, \omega_0, \eta). \end{aligned} \quad (57)$$

Thus we obtain

$$\bar{E}_G^{N-II-SR}(\omega_0, \eta) - \bar{E}_G^{N-II}(\omega_0) = 0, \quad (58)$$

$$\bar{E}_G^{N-II-SR}(\omega_0, \eta) - \bar{E}_G^{SR}(\omega_0) = -\frac{E_F^2 - \omega_0^2}{2E_F}, \quad (59)$$

which are either less than or equal to zero, i.e., the ground state of the N-II-SR mixed phase is stable at $\eta = \eta_c^{(2)}$.

Substituting Eqs (28), (51), and (56) into Eqs (53) and (57), we derive Eqs (45)–(47). In addition, according to Eq. (50), we obtain Eq. (48).

References

- Brennecke, F. *et al.* Cavity QED with a Bose-Einstein condensate. *Nature* **450**, 268–271 (2007).
- Colombe, Y. *et al.* Strong atom-field coupling for Bose-Einstein condensates in an optical cavity on a chip. *Nature* **450**, 272–276 (2007).
- Baumann, K., Guerlin, C., Brennecke, F. & Esslinger, T. Dicke quantum phase transition with a superfluid gas in an optical cavity. *Nature* **464**, 1301–1306 (2010).
- Baumann, K., Mottl, R., Brennecke, F. & Esslinger, T. Exploring Symmetry Breaking at the Dicke Quantum Phase Transition. *Phys. Rev. Lett.* **107**, 140402 (2011).
- Baden, M. P., Arnold, K. J., Grimsmo, A. L., Parkins, S. & Barrett, M. D. Realization of the Dicke Model Using Cavity-Assisted Raman Transitions. *Phys. Rev. Lett.* **113**, 020408 (2014).
- Landig, R., Brennecke, F., Mottl, K., Donner, T. & Esslinger, T. Measuring the dynamic structure factor of a quantum gas undergoing a structural phase transition. *Nat. Commun.* **6**, 7046 (2015).
- Klinder, J., Keßler, H., Reza Bakhtiari, M., Thorwart, M. & Hemmerichl, A. Observation of a Superradiant Mott Insulator in the Dicke-Hubbard Model. *Phys. Rev. Lett.* **115**, 230403 (2015).
- Landig, R. *et al.* Quantum phases from competing short- and long-range interactions in an optical lattice. *Nature* **532**, 476–479 (2016).
- Wang, Y. K. & Hioe, F. T. Phase Transition in the Dicke Model of Superradiance. *Phys. Rev. A* **7**, 831–836 (1973).
- Hioe, F. T. Phase Transitions in Some Generalized Dicke Models of Superradiance. *Phys. Rev. A* **8**, 1440–1445 (1973).
- Ritsch, H., Domokos, P., Brennecke, F. & Esslinger, T. Cold atoms in cavity-generated dynamical optical potentials. *Rev. Mod. Phys.* **85**, 553–601 (2013).
- Kanamoto, R. & Meystre, P. Optomechanics of a Quantum-Degenerate Fermi Gas. *Phys. Rev. Lett.* **104**, 063601 (2010).
- Sun, Q., Hu, X.-H., Ji, A.-C. & Liu, W. M. Dynamics of a degenerate Fermi gas in a one-dimensional optical lattice coupled to a cavity. *Phys. Rev. A* **83**, 043606 (2011).
- Müller, M., Strack, P. & Sachdev, S. Quantum charge glasses of itinerant fermions with cavity-mediated long-range interactions. *Phys. Rev. A* **86**, 023604 (2012).
- Padhi, B. & Ghosh, S. Cavity Optomechanics with Synthetic Landau Levels of Ultracold Fermi Gas. *Phys. Rev. Lett.* **111**, 043603 (2013).
- Guo, X., Ren, Z., Guo, G. & Peng, J. Ultracold Fermi gas in a single-mode cavity: Cavity-mediated interaction and BCS-BEC evolution. *Phys. Rev. A* **86**, 053605 (2012).
- Keeling, J., Bhaseen, M. J. & Simons, B. D. Fermionic Superradiance in a Transversely Pumped Optical Cavity. *Phys. Rev. Lett.* **112**, 143002 (2014).
- Piazza, F. & Strack, P. Umklapp Superradiance with a Collisionless Quantum Degenerate Fermi Gas. *Phys. Rev. Lett.* **112**, 143003 (2014).
- Chen, Y., Yu, Z. & Zhai, H. Superradiance of Degenerate Fermi Gases in a Cavity. *Phys. Rev. Lett.* **112**, 143004 (2014).
- Pan, J.-S., Liu, X.-J., Zhang, W., Yi, W. & Guo, G.-C. Topological Superradiant phases in a Degenerate Fermi Gas. *Phys. Rev. Lett.* **115**, 045303 (2015).
- Chen, Y., Zhai, H. & Yu, Z. Superradiant phase transition of Fermi gases in a cavity across a Feshbach resonance. *Phys. Rev. A* **91**, 021602 (2015).
- Kollath, C., Sheikhan, A., Wolff, S. & Brennecke, F. Ultracold Fermions in a Cavity-Induced Artificial Magnetic Field. *Phys. Rev. Lett.* **116**, 060401 (2016).
- Sheikhan, A., Brennecke, F. & Kollath, C. Cavity-induced chiral phases of fermionic quantum gases. *Phys. Rev. A* **93**, 043609 (2016).
- Sheikhan, A., Brennecke, F. & Kollath, C. Cavity-induced generation of non-trivial topological states in a two-dimensional Fermi gas. *Phys. Rev. A* **94**, 061603(R) (2016).
- Zheng, W. & Cooper, N. R. Superradiance Induced Particle Flow via Dynamical Gauge Coupling. *Phys. Rev. Lett.* **117**, 175302 (2016).
- Cooper, L. N. Bound Electron Pairs in a Degenerate Fermi Gas. *Phys. Rev.* **104**, 1189–1190 (1956).
- Deng, Y., Cheng, J., Jing, H. & Yi, S. Bose-Einstein Condensates with Cavity-Mediated Spin-Orbit Coupling. *Phys. Rev. Lett.* **112**, 143007 (2014).
- Dong, L., Zhou, L., Wu, B., Ramachandran, B. & Pu, H. Cavity-assisted dynamical spin-orbit coupling in cold atoms. *Phys. Rev. A* **89**, 011602 (2014).
- Dimer, F., Estienne, B., Parkins, A. S. & Carmichael, H. J. Proposed realization of the Dicke-model quantum phase transition in an optical cavity QED system. *Phys. Rev. A* **75**, 013804 (2007).
- Fan, J. *et al.* Hidden continuous symmetry and Nambu-Goldstone mode in a two-mode Dicke model. *Phys. Rev. A* **89**, 023812 (2014).
- Dicke, R. H. Coherence in Spontaneous Radiation Processes. *Phys. Rev.* **93**, 99–110 (1954).
- Ford, G. W., Lewis, J. T. & O’Connell, R. F. Quantum Langevin equation. *Phys. Rev. A* **37**, 4419–4428 (1988).
- Scully, M. O. & Zubairy, M. S. *Quantum Optics* (Cambridge University, 1997).
- Larson, J., Morigi, G. & Lewenstein, M. Cold Fermi atomic gases in a pumped optical resonator. *Phys. Rev. A* **78**, 023815 (2008).
- Nagy, D., Szirmai, G. & Domokos, P. Self-organization of a Bose-Einstein condensate in an optical cavity. *Eur. Phys. J. D* **48**, 127–137 (2008).
- Sheehy, D. E. & Radzihovsky, L. BEC-BCS Crossover in “Magnetized” Feshbach-Resonantly Paired Superfluids. *Phys. Rev. Lett.* **96**, 060401 (2006).
- Sheehy, D. E. & Radzihovsky, L. BEC-BCS crossover, phase transitions and phase separation in polarized resonantly-paired superfluids. *Ann. Phys.* **322**, 1790–1924 (2007).
- Sheehy, D. E. Fulde-Ferrell-Larkin-Ovchinnikov phase of two-dimensional imbalanced Fermi gases. *Phys. Rev. A* **92**, 053631 (2015).
- Partridge, G. B., Li, W., Kamar, R. I., Liao, Y.-a. & Hulet, R. G. Pairing and Phase Separation in a Polarized Fermi Gas. *Science* **311**, 503–505 (2006).
- Zwierlein, M. W., Schirotzek, A., Schunck, C. H. & Ketterle, W. Fermionic Superfluidity with Imbalanced Spin Populations. *Science* **311**, 492–496 (2006).
- Kohn, W. & Sham, L. J. Self-Consistent Equations Including Exchange and Correlation Effects. *Phys. Rev.* **140**, A1133–A1138 (1965).
- He, L. & Zhuang, P. Phase diagram of a cold polarized Fermi gas in two dimensions. *Phys. Rev. A* **78**, 033613 (2008).

Acknowledgements

This work is supported in part by the National Key R&D Program of China under Grant No. 2017YFA0304203; the NSFC under Grants No. 11674200, No. 11422433, No. 11604392, No. 11434007, and No. 61378049; the PCSIRT under Grant No. IRT13076; the FANEDD under Grant No. 201316; SFSSSP; OYTPSP; and SSCC.

Author Contributions

Y.F., K.Z., J.F., F.M., G.C., and S.J. conceived the idea, Y.F., K.Z., and J.F. performed the calculation, M.F., G.C., and S.J. wrote the manuscript, F.M. and G.C. supervised the whole research project.

Additional Information

Competing Interests: The authors declare that they have no competing interests.

Publisher's note: Springer Nature remains neutral with regard to jurisdictional claims in published maps and institutional affiliations.



Open Access This article is licensed under a Creative Commons Attribution 4.0 International License, which permits use, sharing, adaptation, distribution and reproduction in any medium or format, as long as you give appropriate credit to the original author(s) and the source, provide a link to the Creative Commons license, and indicate if changes were made. The images or other third party material in this article are included in the article's Creative Commons license, unless indicated otherwise in a credit line to the material. If material is not included in the article's Creative Commons license and your intended use is not permitted by statutory regulation or exceeds the permitted use, you will need to obtain permission directly from the copyright holder. To view a copy of this license, visit <http://creativecommons.org/licenses/by/4.0/>.

© The Author(s) 2017